Lower-Crustal Normal Faulting and Lithosphere Rheology in the Atlas Foreland

Sam Wimpenny[1,2*], Tim Craig[1] and Alice Blackwell[1]

[1]COMET, School of Earth and Environment, University of Leeds, UK

[2]COMET, School of Earth Sciences, University of Bristol, UK

Email: *s.wimpenny@bristol.ac.uk

Abstract

Earthquakes beneath the foreland basins of the Andes and Tibet follow a simple pattern, with normal-faulting events from 0–20 km depth and reverse-faulting events from 30–50 km depth. The switch in faulting style with depth suggests that the elastic stresses generated by flexure within these forelands are large enough to break faults, with opposite senses of horizontal strain either side of a neutral fibre in the mid-crust. In this study, we document a 31 km-deep M_w 5.2 normal-faulting earthquake in the forelands of the Algerian Atlas Mountains near Biskra. The Biskra earthquake is of interest, as it indicates that the lower crust of the Atlas forelands is seismogenic and in extension at the same depth that the Tibetan and Andean forelands are in compression. In order to match the shape of the gravity anomaly and the depth of normal faulting in the Algerian foreland, we find that models of lithospheric flexure require the neutral fibre to be >35 km deep in places and at least the top 5–10 km of the lithospheric mantle supports elastic stresses without yielding. The differences in the depth-extent of normal-faulting earthquakes between the forelands of Tibet, the Andes and the Algerian Atlas can be explained solely by differences in the buoyancy forces acting between these mountain ranges and their lowlands that place the foreland lithosphere into varying amounts of net compression. The upper mantle beneath cratonic foreland lithosphere may therefore support bending stresses of the order of 10's of MPa, likely because it is cool and the strain rates associated with bending are low.

This paper is a pre-print, therefore has not finished peer review and is currently being considered for publication in Earth and Planetary Science Letters.

Highlights:

- We report a 31 km-deep normal-faulting earthquake in the foreland of the Algerian Atlas.
- To account for the gravity anomalies and earthquake depth the lithosphere needs to support elastic stresses 5–10 km below the Moho.
- Differences in the depth of extensional faulting in the forelands of the Atlas, Andes and Tibet can be explained by different in-plane compressional forces.

1 Introduction

Bending of the foreland lithosphere along the margins of mountain ranges sets up differential stresses that are supported over geological timescales ($\sim 10^6$ yr) by resistance to deformation. It is generally agreed that within the cratonic lithosphere surrounding high mountain ranges the stresses generated by bending are supported in a single, strong layer underlain by a weaker layer [Jackson, 2002; Watts and Burov, 2003]. However, in one model this strong layer is 30–50 km-thick, corresponds roughly to the crustand the bending stresses are everywhere close to the yield strength of the lithosphere apart from within a thin (<10 km) elastic core [Jackson, 2002]. The alternative model is that bending stresses are supported over a >60 km-thick layer that extends well into the lithospheric mantle, and the stresses are mostly far below the lithosphere's yield strength [Watts and Burov, 2003]. One of the key difference between these two models lies in the whether the continental lithospheric mantle is, or is not, strong enough to support significant (i.e. 10's of MPa) bending stresses.

An important observation in this debate is that a small number of well-recorded $M_w > 5$ normal-faulting earthquakes with nodal planes parallel to mountain range fronts have been observed between the surface and 20 km depth in the forelands of Tibet and the Andes [e.g. Baranowski et al., 1984; Priestley et al., 2008; Wimpenny, 2022]. Reverse-faulting earthquakes are also observed in the same regions, but with centroid depths of 30–50 km in the lower crust and potentially the upper-most few kilometers of the lithospheric mantle [e.g. Priestley et al., 2008; Devlin et al., 2012]. The same pattern of extensional earthquakes at 0–30 km depth overlaying compressional earthquakes at 35–50 km depth is observed globally within oceanic lithosphere as it bends at the outer-trench slope adjacent to subduction zones [Chapple and Forsyth, 1979; Craig et al., 2014]. In both the oceans and continents, the switch from a single layer of extensional earthquakes to a single layer of compressional earthquakes with depth has been interpreted to reflect the release of elastic stresses generated by bending strains, with a 'neutral fibre' lying in between the seismogenic portions of the lithosphere where the bending strains are small [Chapple and Forsyth, 1979; Jackson, 2002].

The neutral fibre depth within the forelands of Tibet lies at 20–25 km, roughly in the middle of the crust. Jackson [2002] argued that the simplest interpretation of this observation is that the majority of the strength of the foreland lithosphere bounding Tibet lies within the seismogenic crust, and that the aseismic upper mantle supports little stress as it deforms through temperature-controlled crystal-plastic creep. However, it is also possible that the neutral fibre could be shifted shallower than the middle of the strong layer due to the range-perpendicular compressional force that acts through mountain range forelands [Molnar and Lyon-Caen, 1988]. As a result, significant bending stress could still be supported by the lithospheric mantle. The rarity of earthquakes beneath foreland basins due to the low strain rates caused by bending in the continents ($< 10^{-17}$ 1/s), particularly in the forelands of lower elevation mountain ranges that possibly have smaller in-plane compressional forces, has limited our ability to test these two competing hypotheses.

In this study, we report an unusually deep M_w 5.2 normal-faulting earthquake that occurred on the 18th November 2016 within the forelands of the southern Atlas Mountains near Biskra, Algeria (Figure 1). Our analysis of the teleseismic body-waves from this earthquake in Section 3 places the centroid at 31 km depth near the foreland Moho and, notably, 11 km deeper than any previously recognised normal-faulting earthquake beneath a continental foreland basin. The depth and focal mechanism of the Biskra earthquake are unusual because it indicates that the foreland lower crust is undergoing range-perpendicular extension, which contrasts with the compressional earthquakes observed at similar depths beneath the foreland basins that wrap around the margins of Tibet and the Andes. The purpose of this study is two-fold. First, we examine what range of lithosphere rheologies can account for the observations of flexure, and the depth and mechanism of the Biskra earthquake, within the Atlas foreland. Second, we explore the possible causes of differences in the depth distribution of bending-related earthquakes between the forelands of the Atlas, Andes and Tibet.

2 Tectonic Context

The Biskra earthquake occurred south of the range front of the Aurés Mountains, which form a part of the Atlas mountain chain of North Africa near the Algerian-Tunisia border (Figure 1a). The epicentral region is associated with an asymmetrical free-air gravity low of amplitude ∼50 mGal that has its maximum running parallel to the range front and that extends ∼200 km from the range front into the Saharan Platform (Figure 1b). The shape of the anomaly is typical of those seen globally along the margins of mountain belts caused by low-density sediments filling in a flexural depression, and can be fit by a simple model of a thin, bending plate with an effective elastic thickness T_e of at least 20 km and a plate curvature of 1–4$\times 10^{-7}$ 1/m using the forward-modelling approach of McKenzie and Fairhead [1997] (Figure 1b).

The geological history of the region around Biskra is also consistent with the northern margin of the Saharan Platform bending due to the load of the Atlas. Surface exposure within the Aurés Mountains records a history of Mesozoic rifting during the break-up of Pangea that occurred in multiple phases between the Permian and early Cretaceous [Bracene et al., 2003]. These rift sediments were then shortened as Africa drifted northwards relative to Eurasia in the Cenozoic, with the most recent major phase of shortening deforming Pleistocene sediments along the southern margin of the Aurés Mountains [Frizon de Lamotte et al., 2000]. Gentle folding of Quaternary river sediments [Frizon de Lamotte et al., 2000] and GPS measurements [Bougrine et al., 2019] suggest that the range front is still active south-east of Biskra and is shortening at a rate of 1–3 mm/yr with a component of range-parallel right-lateral motion (Figure 1c). The mechanisms of shallow (i.e. <10 km) reverse and strike-slip faulting earthquakes near the range front support this view (Figure 1c). Whilst the Cenozoic rocks within the Aurés Mountains record a history of tectonic shortening, Cenozoic rocks on the Saharan Platform consist of a 1–2 km-thick sedimentary succession that has remained mostly undeformed and thickens towards the range front [Frizon de Lamotte et al., 2000; Underdown and Redfern, 2008]. The geometry of these sediments, and their subsidence histories, are indicative of deposition in a foreland basin setting [Underdown and Redfern, 2008].

3 Body-Waveform Modelling of the 2016 Biskra Earthquake

The Biskra earthquake occurred at 07:42 UTC on the 18th November 2016 with a centroid determined by the global Centroid Moment Tensor (gCMT) catalogue at 24 km depth [Ekström et al., 2012] and a hypocentre in the ISC-EHB catalogue at 21 km depth [Weston et al., 2018]. Routine earthquake depth estimates from the gCMT and ISC-EHB may carry significant errors and uncertainties, particularly for shallow events within the crust, because of the limited sensitivity of long-period waveforms and direct-phase travel times to earthquake depths [e.g. Maggi et al., 2000]. Therefore, we manually re-analysed the teleseismic waveforms of the Biskra earthquake to determine its depth, focusing particularly on identifying surface-reflected depth phases within the P-wave coda.

The P-wave first arrivals on vertical-component seismograms at teleseismic distances (30–90°) and at all back-azimuths had dilatational arrivals, with those at the north-eastern most stations having low-amplitude first arrivals suggesting they are near nodal (Figure 2a). Potential phase arrivals were also evident within the P-wave coda 10–15 seconds after the P-wave arrival (Figure 2a). We first beamformed the vertical-component waveforms measured at the small-aperture seismic arrays at Kurchatov (KU: Kazhakstan), Yellowknife (YK: Canada) and Pinedale (PD: USA) to confirm that the energy within the coda at 10–15 s derived from the same back-azimuth as the mainshock (Supplementary Figure 1). We also performed beamforming and phase-weighted stacking of vertical-component waveforms across a medium-aperture sub-array of stations at 40.3 epicentral degrees from the source, which demonstrates that the arrivals are also coherent in slowness and have the opposite polarity to the direct arrival in this epicentral distance range (Figure 2b). The arrival times of the coda phases relative to the direct P-wave do not move-out significantly as a function of epicentral distance, and the phases appear as a pair at station ATD (Figure 2a) and in the medium-aperture array analysis (Figure 2b). We interpret these arrivals to be the principal surface-reflected depth phases pP and sP.

To determine the centroid depth of the Biskra earthquake we modelled the waveforms of the P, pP and sP phases assuming the earthquake source can be approximated by an instantaneous rupture at a point in space using the WKBJ algorithm of Chapman [1978] and the ak135 velocity model of Kennett et al. [1995]. We applied a t^* attenuation filter [Futterman, 1962] and a zero-phase bandpass filter between 0.5 Hz and 2.0 Hz to both the synthetic and observed waveforms to remove high-frequency features related to source-time function and noise [see Maggi et al., 2000]. We found that the gCMT mechanism satisfied the majority of the P-wave arrival polarities and relative amplitudes, but the north-dipping nodal plane needed to have a $\sim$10° steeper dip to account for the low amplitude P-wave arrivals recorded at stations north of the earthquake epicentre. For this updated mechanism the best fit between the synthetics and the observed waveforms occurred at a centroid depth of 31 km (Figure 2a), with an uncertainty related to waveform matching of $\pm$1 km. The best-fit centroid depth is 7 km deeper than the gCMT estimate, which has only a minor effect on the predicted take-off angles and is therefore likely to have only a minor effect on the best-fit earthquake mechanism [Craig et al., 2023].

Uncertainties of $\pm$10% in V_p and V_s above the earthquake centroid contribute a further $\pm$2 km of uncertainty, yielding a centroid depth estimate in the range 28–34 km. The Moho depth in the region has been mapped through deep seismic soundings conducted by the European Geotraverse at $\sim$34–38 km in the foreland of the Tunisian Atlas [Morelli and Nicolich, 1990]. Therefore, the Biskra earthquake demonstrates that the lower crust is seismogenic and in range-perpendicular extension along the northern margin of the Saharan Platform in Algeria.

3.1 Tectonic Interpretation

Active reverse faulting within and along the margins of the Atlas Mountains suggests that the stresses within the lithosphere are dominantly associated with NNW–SSE compression [Heidbach et al., 2010]. Buoyancy forces acting between the Atlas Mountains and the Saharan Platform are also likely to place the foreland into range-normal compression in the absence of other forces [Molnar and Lyon-Caen, 1988]. However, the normal-faulting mechanism of the Biskra earthquake is not consistent with a range-normal compressional stress state.

One potential explanation for the normal-faulting mechanism of the Biskra earthquake is that it is associated with localised transtension along the range front, but this is not supported by the GPS velocities measured either side of the earthquake epicentre (see Figure 1a). We hypothesise that the horizontal stresses generated by flexure of the Saharan Platform may be large enough to adjust the stress state and place the lower crust into a state of range-normal extension. We explore this possibility below using analytical and numerical modelling of lithospheric flexure.

4 Modelling of the Stresses in the Atlas Foreland

The Biskra earthquake occurred in a section of the Saharan Platform with a free-air gravity low that runs parallel to the Atlas range front for 400 km along-strike. The earthquake also had a mechanism with both nodal planes sub-parallel to the Atlas range front (Figure 1a). Based on the shape of the gravity anomalies, we simplify our analysis of the stresses within the Saharan Platform generated by flexure to two-dimensional plane stress, and assume that strains along-strike are negligible. We also make the assumption that the strong part of the flexed lithosphere is thin relative to the wavelength of flexure ($\sim$200 km in Figure 1a) and the bending strains are small. Under these standard assumptions the deflection of the lithosphere's surface can be approximated by the theory of a thin, bending plate overlying an inviscid half-space subject to forces and bending moments on its edge [e.g. Turcotte and Schubert, 2002]. The differential stresses within the plate $\Delta\sigma_{xx} = \sigma_{xx} - \sigma_{zz}$ are related to the bending moment M and in-plane force F_x:

$$M(x) = \int_0^{z_l} z' \Delta\sigma_{xx}(x)\, dz \tag{1}$$

$$F_x = \int_0^{z_l} \Delta\sigma_{xx}(x)\, dz \tag{2}$$

where z_l is the thickness of the plate and z' is the distance from the neutral fibre. Equations 1 and 2 are independent of the assumed plate rheology or boundary conditions [Turcotte and Schubert, 2002]. In what follows, we use the convention that positive differential stresses ($\sigma_{xx} > \sigma_{zz}$) are associated with a stress state that promotes extensional faulting.

Faulting within the foreland lithosphere suggest that some fraction of the bending strains are accommodated through plastic (non-recoverable) deformation. We therefore model the stress-strain due to flexure as an elastic perfectly-plastic process [McAdoo et al., 1978]. From the surface down to a depth H, we assume that stress in the plate can build up elastically but is limited by the frictional resistance to slip on faults dipping at 45° (the 'brittle layer') [Goetze and Evans, 1979]. We interpret the Biskra earthquake to indicate that the plate can remain brittle to at least 31±3 km depth.

Beneath the brittle layer, as temperature in the lithosphere increases with depth, crystal-plastic deformation mechanisms including low-temperature plasticity and dislocation creep will limit the size of the elastic stresses [Goetze and Evans, 1979]. These creep mechanisms are strain-rate dependent, but the axial strain rates associated with flexure in Algeria will be small (10^{-19}–10^{-21} 1/s) given the small curvatures (1–4$\times10^{-7}$ 1/m) and underthrusting rates (1–3 mm/yr) in the foreland. Supplementary Figure 2 shows predictions of the stress needed to deform a lithospheric mantle formed of dry olivine at the strain rates caused by bending. For the expected range of differential stresses (<500 MPa) and at depths >30 km the stresses in the mantle are limited by dislocation creep and can be approximated by a function of the form $\sigma_0 \exp(-z/z_r)$ where $z_r \approx 5$ km [Lavier and Steckler, 1997]. Therefore, we make the simplification that the limit on the elastic stresses below the brittle layer follows an exponential decay down to the base of the plate, and present results of modelling with different assumed z_r.

The rheological model described above replicates the single-layer model for cratonic lithosphere [Jackson, 2002; Watts and Burov, 2003]. We do not consider a multi-layer rheology with widespread ductile yielding in a weak lower crust bracketed by a strong, brittle layer above and below [Burov and Diament, 1995] because the Biskra earthquake suggests that the elastic stresses that can build up in the lower crust are limited by resistance to slip on faults.

We have also not included any visco-elastic effects [e.g. Kusznir, 1991; Ellis and Wang, 2022] and assume that the deflection of the lithosphere can be modelled by static loading. Visco-elasticity has the effect of introducing time-dependence to the stress distribution following the application of a load, such that stresses associated with past episodes of loading can remain 'frozen in' to the lithosphere.

Ellis and Wang [2022] showed that the time-scale for the change in stress state within the cold, elastic portion of cratonic lithosphere following a change in horizontal loading is on the order of ∼5–10 Myrs. Given that the Atlas and its forelands have been undergoing shortening and loading in the current tectonic configuration throughout the Cenozoic, and given that we are not trying to derive the values of the loads but rather the stresses within the plate, then we believe it is reasonable to model the loads using a static approximation.

4.1 Analytical Modelling

The depth of normal-faulting earthquakes within the foreland lithosphere places a bound on the depth to which the stresses generated by flexure are equivalent to the stresses needed to break normal faults ('extensional yielding'). To gain insight into the controls on the depth of extensional yielding, we constructed a semi-analytical model using Equations 1–2, plus the condition that the plate curvature is related to the stress gradient within the plate's elastic core [e.g. Lavier and Steckler, 1997]:

$$\frac{d^2w}{dx^2} = \frac{(1-v^2)}{E}\frac{d\Delta\sigma_{xx}}{dz}, \tag{3}$$

where w is the deflection, $E = 70$ GPa is Young's modulus, and $v = 0.25$ is Poisson's ratio. From Equations 1–3, if the curvature of the lithosphere and the in-plane force F_x can be estimated, then we can determine the relationships between the depth of extensional yielding and the parameters that control the lithosphere's rheology (H, μ', z_r) in our simplified model set-up. The resulting solutions are semi-analytical, as we solve Equations 1–2 using numerical integration.

For the modest plate curvatures in the Saharan Platform on the southern margin of the Atlas mountains (∼3×10^{-7} 1/m), the depth of extensional yielding is mostly dependent on the brittle-layer thickness H and less so on the effective frictional strength of faults within the brittle layer μ' (Figure 3a). For brittle layers similar in thickness to typical foreland crust (∼30–40 km), extensional yielding can occur down to ∼10–25 km depth for $\mu' = 0.1$–0.6. Increasing the stresses supported in the lithospheric mantle by increasing z_r has the effect of increasing the depth of extensional yielding for a fixed F_x (Figure 3a), because of the need to balance the larger contribution of bending stresses to the bending moment below the neutral fibre (Equation 1). For the equivalent H-μ' range, but with an in-plane compression of 2 TN/m that simulates a small buoyancy force acting between the mountains and forelands, the neutral fibre is shifted shallower and the depth of extensional yielding decreases to 10–15 km (Figure 3b). A tensional in-plane force would increase the depth of extensional yielding, but this scenario is unlikely in a foreland setting.

These simple calculations demonstrate that, if the Saharan Platform is in net compression, then for the estimated plate curvature no models have a depth of extensional yielding of ~30 km in a brittle layer H that is similar in thickness to the crust (34–38 km; Morelli and Nicolich [1990]). The lithospheric mantle may therefore need to support a fraction of the differential stresses generated by flexure in the Atlas foreland to account for the depth of the Biskra earthquake.

4.2 Numerical Modelling

In practice the stress distribution within the lithosphere will vary as a function of distance from the range front in tandem with variations in the plate curvature. In this section, we employ a simple two-dimensional numerical model of plate bending in response to static loading to determine the range of lithosphere rheologies that can account for both the shape of the free-air gravity anomalies, which reflect the plate curvature, and the depth of normal faulting in the Saharan Platform.

We model the bending of a thin plate subject to arbitrary end-loads and moments following Burov and Diament [1992], and solve the relevant equations of plate flexure using the open-source finite-difference code tAo [Garcia-Castellanos et al., 1997]. On the foreland boundary of the model x_{max}, we apply the condition that $w(x = x_{max}) = 0$. Along the boundary of the plate beneath the mountains x_0, we apply the condition that the vertical shear force V on the plate end is $V(x = x_0) = 0$, which is equivalent to assuming the plate is broken. The range front is positioned at $x = 0$. We also tested models with a continuous plate boundary condition (i.e. $w'(x = x_0) = 0$), though found it did not change the model results as the best-fit position of x_0 was typically far from the range front ($x_0 \ll 0$). We computed gravity anomalies from the modelled deflection using the plate approximation $\Delta g(x) = 2\pi G \Delta\rho w(x)$, where G is the gravitational constant and $\Delta\rho$ is the density contrast between basin sediment and mantle (see a sketch of the model set-up in Supplementary Figure 3).

To determine the range of models that match the gravity and earthquake observations, we performed a Montle Carlo search of the parameter space with a non-linear least-squares minimisation step to solve for nuisance parameters. The free parameters were the vertical force acting on the edge of the plate $F_z(x = x_0)$, the in-plane force F_x, bending moment $M(x = x_0)$, the location of the plate break x_0, the density contrast between basin sediment and mantle $\Delta\rho$, and the brittle layer thickness H and effective static friction of faults μ' (see Table 1 for parameter ranges). We assumed that the foreland is in horizontal net compression due to the buoyancy forces acting between the Atlas Mountains and Saharan Platform. The nuisance parameters consist of a static offset and linear ramp added to the modelled gravity data to account for long-wavelength contributions to the gravity field from mantle flow. We searched over 1 million different combinations of parameters, and stored the models that match the gravity data with $\chi^2 \leq 1.5\chi^2_{min}$ and which experienced plastic yielding in horizontal extension at >28 km depth south of the range front. Increasing the number of parameter combinations did not change the range of models that matched the data, suggesting the inferences we draw from this sample are robust.

We find that plate models can match the gravity data to within the uncertainty bound as long as $H \geq 20$ km (Figure 4a). The largest misfits between the models and observations occur within 20–40 km of the range front where the gravity anomaly has an inflexion to become concave up, which most likely represents aliasing of the positive free-air gravity high in the mountains with the free-air gravity low in the foreland basin. By including the constraint that the models need to match both the gravity data and the depth of extensional yielding inferred from the Biskra earthquake, the brittle layer H needs to be >40 km thick and contain faults with $\mu' > 0.025$ (Figure 4b,c). The models constrain the lower bound on the brittle layer thickness for two reasons. Firstly, by selecting models with extensional yielding down to >28 km depth we implicitly assume the brittle layer must be at least this thick. Secondly, the lithosphere needs to be strong enough to match the shape of the gravity anomalies. Lithosphere with a brittle layer less than 40 km thick, and which is yielding at >28 km depth, produces a short-wavelength deflection that is not consistent with the shape of the observed free-air gravity anomaly. The lower bounds the numerical models place on H and μ' are similar to those inferred from the semi-analytical models in Section 4.1, and require that at least the top 5–10 km of the lithospheric mantle beneath the Saharan Platform supports bending-related stresses through elastic resistance to deformation. A compilation of the stress distributions at the point within the foreland where the depth of extensional yielding is at its maximum shows that, immediately below the Moho, these elastic stresses are at least $\sim$40 MPa (Figure 4d).

Increasing the brittle layer thickness beyond 40 km has little effect on the model fits, because thicker britltle layers are able to match the gravity data and depth of extensional yielding by increasing the forces deforming the lithosphere, reducing the effective friction, by having larger distances to the load point x_0, or by a combination of these three factors (Supplementary Figure 4). These various trade-offs mean that, similar to the forward modelling approaches for estimating the effective elastic thickness from gravity profiles [e.g. McKenzie and Fairhead, 1997], we cannot constrain the upper bound on the brittle layer thickness. Similarly, we cannot place any upper bound on the amplitude of the differential stresses within the crust or lithospheric mantle caused by bending.

5 Discussion

Our modelling of the stress distribution within the Atlas foreland places useful new constraints on the rheology of the continental lithosphere in northern Africa, and on the geodynamics of flexural foreland regions worldwide. In order to account for the depth of extensional faulting near Biskra, we find that the lithospheric mantle of the Saharan Platform needs to support bending stresses on the order of a few 10's of MPa elastically down to depths at least 5–10 km below the Moho. In addition, the Biskra earthquake demonstrates that the lower crust beneath the Saharan Platform is seismogenic, and therefore needs to be able to sustain enough elastic stress to rupture faults.

The constraints on the rheology of the Saharan Platform are similar to those determined for the Indian lithosphere where it underthrusts the southern margin of Tibet. Within the Indian lithosphere, earthquakes have been found to occur throughout the crust [Bodin and Horton, 2004] and are now believed to extend up to $\sim$10 km below the Indian Moho beneath the Himalaya [Craig et al., 2012; Schulte-Pelkum et al., 2019], indicating that the lower crust and upper mantle is able to accumulate and release elastic strain in earthquakes at stresses lower than those needed to deform by crystal-plastic creep. The Indian lithosphere is thought to be strong enough to accumulate elastic stresses into the upper mantle through the combination of a relatively thin, anhydrous crust, and a cold uppermost mantle, thermally (and possibly chemically) insulated from the hot convecting mantle by a $\sim$200 km-thick lithospheric keel [Priestley et al., 2008]. Recently published multi-mode surface-wave tomography shows that the similarly thick lithosphere previously known to underlie the West African Craton also extends beneath the southern Atlas foreland and is 150–180 km-thick beneath Biskra [Priestley and McKenzie, 2013; Celli et al., 2020]. We constructed geotherms using the lithosphere and crustal thickness estimates near Biskra and, for the expected axial strain rates associated with bending (10^{-19}–10^{-21} 1/s), laboratory-derived flow laws for dry olivine [Hirth and Kohlstedt, 2003; Mei et al., 2010] predict that the top 10 km of the lithospheric mantle of the Saharan Platform could well be cool enough to support differential stresses of a few 10's of MPa elastically (Supplementary Figure 5). However, the range of models in which elastic stresses of 100's of MPa are supported within the upper mantle appear unlikely even if it is formed of dry olivine, as the required bending strains could be accommodated at differential stresses $\ll$100 MPa by dislocation creep. Importantly, these results indicate that the lithospheric mantle does support a significant fraction of the bending stresses in the Algerian foreland lithosphere, even though the strain rates associated with bending are at least 1 order of magnitude less than those in the Indian lithosphere as it underthrusts Tibet.

If the lithosphere surrounding the margins of Tibet and the Andes has a similar rheology to the Saharan Platform, this raises the question: why is the depth of extensional faulting so much deeper in the Atlas foreland? One of the key differences between the Tibetan, Andean and Atlas forelands is the amplitude of the buoyancy force that places the foreland lithosphere into net compression [Molnar and Lyon-Caen, 1988]. These buoyancy forces derive predominantly from contrasts in crustal thickness between the mountain range and its forelands, and are roughly proportional to the height h of the mountain range squared [Molnar and Lyon-Caen, 1988]. Estimates of the buoyancy force acting through the Indian lithosphere are on the order of 5–6 TN/m (h = 5000 m) [Copley et al., 2010], within the Brazilian Shield near the central Andes they are 4–6 TN/m (h = 4500 m) [Lamb, 2000], and within the northern Andes they are 3–4 TN/m (h = 3000 m) [Wimpenny, 2022]. A similar calculation for the Atlas Mountains, which has an average elevation of h = 1500 m, results in a buoyancy force of 1–2 TN/m. If larger buoyancy forces equate to a larger in-plane compression acting through the adjacent forelands, then forelands of high mountains may be expected to have a shallower neutral fibre and shallower normal faulting seismicity. We performed a simple test of this hypothesis using the semi-analytical modelling approach described in Section 4.1.

We selected the four continental foreland basins that have well-recorded normal-faulting seismicity (see Table 2), and calculated the range of plausible plate curvatures from the free-air gravity anomalies (Supplementary Figures 6–8). We then assumed that the buoyancy forces acting between the mountains and lowlands are equivalent to the in-plane force F_x, and computed the depth of extensional and compressional yielding as a function of the brittle layer thickness H and effective friction of faults μ' in the brittle layer. Figure 5a shows the range of H-μ' that is consistent with the observed depth-extent of normal and reverse faulting in each foreland. The depth distribution of seismicity in all four settings can be explained if the lithosphere has $\mu' \approx 0.025$–0.1 and $H \gtrsim 50$ km (Figure 5a). The small size of the region of overlap in Figure 5a is somewhat artificial, as it is sensitive to the assumptions about the uncertainties in the depth of earthquakes and the shape of the yield strength envelope in the lithospheric mantle. Nevertheless, these simple calculations demonstrate that if the upper ∼10–20 km of the lithospheric mantle is able to support bending stresses, then a smaller in-plane compression in the forelands of the Atlas compared to that in the forelands of Tibet and the Andes provides a simple explanation for the differences in the depth of extensional faulting between these settings (Figure 5b).

6 Conclusions

The 2016 Biskra normal-faulting earthquake was unusual in that it ruptured the lower crust of the foreland lithosphere bounding the Algerian Atlas Mountains. We have shown that simple models of lithospheric flexure can account for the depth and mechanism of the Biskra earthquake and gravity anomalies within the region, but indicate that at least the top 5–10 km of the foreland lithospheric mantle support bending stresses of a few 10's of MPa elastically. The southern margin of the Atlas is underlain by moderately thick lithosphere, which may lead to a cool and thereby strong upper mantle that can support these bending stresses, even at the low axial strain rates associated with the underthrusting of the Saharan Platform beneath the Atlas Mountains (10^{-19}–10^{-21} 1/s). Differences in the depth distribution and mechanisms of earthquakes between the forelands of the Andes, Tibet and the Atlas can be explained if these foreland regions have similar rheologies but have different in-plane compressional forces that are roughly equivalent to the buoyancy forces acting between the mountains and their lowlands. Our findings indicate that the strong continental lithosphere bounding mountain ranges supports significant differential stresses within at least the top few tens of kilometers of the upper mantle.

Acknowledgements

SW and TJC were supported in this work by the Royal Society under URF\R1\180088 and RF\ERE\210041, and also through COMET, which is the NERC Centre for the Observation and Modelling of Earthquakes, Volcanoes and Tectonics, a partnership between UK Universities and the British Geological Survey. AB was supported by the Leeds-York-Hull Natural Environment Research Council (NERC) Doctoral Training Partnership (DTP) Panorama under grant NE/S007458/1. The numerical modelling component of this work was undertaken on ARC4, part of the High Performance Computing facilities at the University of Leeds, UK.

Data Availability

All data used in this study are openly available. Seismic data are freely available from IRIS at `https://ds.iris.edu/wilber3`, and the modelling code tAo is available from `https://sites.google.com/site/daniggcc/software/tao` (last accessed May 2023). All of the codes needed to reproduce the modelling results are available from [INSERT ZENODO LINK ON PUBLICATION].

References

Baranowski, J., Armbruster, J., Seeber, L., and Molnar, P. (1984). Focal depths and fault-plane solutions of earthquakes and active tectonics of the Himalaya. *Journal of Geophysical Research*, 89(B8):6918–6928.

Bodin, P. and Horton, S. (2004). Source Parameters and Tectonic Implications of Aftershocks of the Mw 7.6 Bhuj Earthquake of 26 January 2001. *Bulletin of the Seismological Society of America*, 94(3):818–827.

Bougrine, A., Yelles-Chaouche, A. K., and Calais, E. (2019). Active deformation in Algeria from continuous GPS measurements. *Geophysical Journal International*, 217(1):572–588.

Bracene, R., Patriat, M., Ellouz, N., and Gaulier, J. M. (2003). Subsidence history in basins northern Algeria. *Sedimentary Geology*, 156(1-4):213–239.

Burov, E. B. and Diament, M. (1992). Flexure of the continental lithosphere with multilayered rheology. *Geophysical Journal International*, 109(2):449–468.

Burov, E. B. and Diament, M. (1995). The effective elastic thickness (Te) of continental lithosphere: What does it really mean? *Journal of Geophysical Research: Solid Earth*, 100(B3):3905–3927.

Celli, N. L., Lebedev, S., Schaeffer, A. J., Ravenna, M., and Gaina, C. (2020). The upper mantle beneath the South Atlantic Ocean, South America and Africa from waveform tomography with massive data sets. *Geophysical Journal International*, 221(1):178–204.

Chapman, C. H. (1978). A new method for computing synthetic seismograms. *Geophysical Journal International*, 54(3):481–518.

Chapple, W. M. and Forsyth, D. W. (1979). Earthquakes and Bending of Plates at Trenches. *Journal of Geophysical Research*, 84(B12):6729–6749.

Copley, A., Avouac, J. P., and Royer, J. Y. (2010). India-Asia collision and the Cenozoic slowdown of the Indian plate: Implications for the forces driving plate motions. *Journal of Geophysical Research: Solid Earth*, 115(3):1–14.

Craig, T. J., Copley, A., and Jackson, J. A. (2012). Thermal and tectonic consequences of India underthrusting Tibet. *Earth and Planetary Science Letters*, 353-354:231–239.

Craig, T. J., Copley, A., and Middleton, T. A. (2014). Constraining fault friction in oceanic lithosphere using the dip angles of newly-formed faults at outer rises. *Earth and Planetary Science Letters*, 392:94–99.

Craig, T. J., Jackson, J., Priestley, K., and Ekström, G. (2023). A Cautionary Tale: examples of the mis-location of small earthquakes beneath the Tibetan plateau by routine approaches. *Geophysical Journal International*, 233(3):2021–2038.

Devlin, S., Isacks, B. L., Pritchard, M. E., Barnhart, W. D., and Lohman, R. B. (2012). Depths and focal mechanisms of crustal earthquakes in the central Andes determined from teleseismic waveform analysis and InSAR. *Tectonics*, 31(2):1–33.

Ekström, G., Nettles, M., and Dziewoński, A. (2012). The global CMT project 2004–2010: Centroid-moment tensors for 13,017 earthquakes. *Physics of the Earth and Planetary Interiors*, 200:1–9.

Ellis, S. and Wang, K. (2022). Lithospheric strength and stress revisited: Pruning the Christmas tree. *Earth and Planetary Science Letters*, 595:117771.

Frizon de Lamotte, D., Saint Bezar, B., Bracene, R., and Mercier, E. (2000). The two main stepsof the Atlas building and geodynamics of the western Mediterranean. *Tectonics*, 19(4):740–761.

Futterman, W. I. (1962). Dispersive body waves. *Journal of Geophysical Research*, 67(13):5279–5291.

Garcia-Castellanos, D., Fernàndez, M., and Torne, M. (1997). Numerical modeling of foreland basin formation: A program relating thrusting, flexure, sediment geometry and lithospehre rheology. *Computers and Geosciences*, 23(9):993–1003.

Goetze, C. and Evans, B. (1979). Stress and temperature in the bending lithosphere as constrained by experimental rock mechanics. *Geophysical Journal of the Royal Astronomical Society*, 59(3):463–478.

Heidbach, O., Tingay, M., Barth, A., Reinecker, J., Kurfeß, D., and Müller, B. (2010). Global crustal stress pattern based on the World Stress Map database release 2008. *Tectonophysics*, 482(1-4):3–15.

Hirth, G. and Kohlstedt, D. L. (2003). Rheology of the Upper Mantle and the Mantle Wedge: a View From the Experimentalists. *Geophysical Monograph Series*, 138:83–106.

Jackson, J. A. (2002). Strength of the continental lithosphere: Time to abandon the jelly sandwich? *GSA Today*, 12(9):4.

Kennett, B. L. N., Engdahl, E. R., and Buland, R. (1995). Constraints on seismic velocities in the Earth from traveltimes. *Geophysical Journal International*, 122(1):108–124.

Kusznir, N. J. (1991). Time distribution of stress with depth in the lithosphere: thermo- rheological and geodynamic constraints. *Philosophical Transactions - Royal Society of London, A*, 337(1645):95–110.

Lamb, S. H. (2000). Active deformation in the Bolivian Andes, South America. *Journal of Geophysical Research: Solid Earth*, 105(B11):25627–25653.

Laske, G. and Masters, G. (1997). A Global Digital Map of Sediment Thickness. *Eos, Transactions American Geophysical Union*, 78.

Lavier, L. L. and Steckler, M. (1997). The effect of sedimentary cover on the flexural strength of continental lithosphere. *Nature*, 389:476–479.

Maggi, A., Jackson, J. A., McKenzie, D., and Priestley, K. (2000). Earthquake focal depths, effective elastic thickness, and the strength of the continental lithosphere. *Geology*, 28(6):495.

McAdoo, D. C., Caldwell, J. G., and Turcotte, D. L. (1978). On the elastic-perfectly plastic bending of the lithosphere under generalized loading with application to the Kurd Trench. *Geophysical Journal of the Royal Astronomical Society*, 54(1):11–26.

McKenzie, D. and Fairhead, D. (1997). Estimates of the effective elastic thickness of the continental lithosphere from Bouguer and free air gravity anomalies. *Journal of Geophysical Research: Solid Earth*, 102(B12):27523–27552.

Mei, S., Suzuki, A. M., Kohlstedt, D. L., Dixon, N. A., and Durham, W. B. (2010). Experimental constraints on the strength of the lithospheric mantle. *Journal of Geophysical Research: Solid Earth*, 115(B8):B08204.

Molnar, P. and Lyon-Caen, H. (1988). Some simple physical aspects of the support, structure, and evolution of mountain belts. In *Geological Society of America Special Papers*, volume 218, pages 179–208. Geological Society of America.

Morelli, C. and Nicolich, R. (1990). A cross section of the lithosphere along the European Geotraverse Southern Segment (from the Alps to Tunisia). *Tectonophysics*, 176(1-2):229–243.

Priestley, K., Jackson, J. A., and Mckenzie, D. (2008). Lithospheric structure and deep earthquakes beneath India, the Himalaya and southern Tibet. *Geophysical Journal International*, 172(1):345–362.

Priestley, K. and McKenzie, D. (2013). The relationship between shear wave velocity, temperature, attenuation and viscosity in the shallow part of the mantle. *Earth and Planetary Science Letters*, 381:78–91.

Schulte-Pelkum, V., Monsalve, G., Sheehan, A. F., Shearer, P., Wu, F., and Rajaure, S. (2019). Mantle earthquakes in the Himalayan collision zone. *Geology*, 47(9):815–819.

Shako, R., Forste, C., Abrikosov, O., Bruinsma, S., Marty, J.-C., Lemoine, J.-M., Flechtner, F., Neumayer, H., and Dahle, C. (2014). EIGEN-6C: A High-Resolution Global Gravity Combination Model Including GOCE Data. *Observation of the System Earth from Space - CHAMP, GRACE, GOCE and future missions*, pages 155–161.

Turcotte, D. L. and Schubert, G. (2002). *Geodynamics*. Cambridge University Press.

Underdown, R. and Redfern, J. (2008). Petroleum generation and migration in the Ghadames Basin, north Africa: A two-dimensional basin-modeling study. *American Association of Petroleum Geologists Bulletin*, 92(1):53–76.

Watts, A. B. and Burov, E. B. (2003). Lithospheric strength and its relationship to the elastic and seismogenic layer thickness. *Earth and Planetary Science Letters*, 213(1-2):113–131.

Weston, J., Engdahl, E. R., Harris, J., Di Giacomo, D., and Storchak, D. A. (2018). ISC-EHB: Reconstruction of a robust earthquake data set. *Geophysical Journal International*, 214(1):474–484.

Wimpenny, S. (2022). Weak, Seismogenic Faults Inherited From Mesozoic Rifts Control Mountain Building in the Andean Foreland. *Geochemistry, Geophysics, Geosystems*, 23(3):1–19.

Wimpenny, S. and Watson, C. S. (2020). gWFM: A global catalog of moderate-magnitude earthquakes studied using teleseismic body waves. *Seismological Research Letters*, 92(1):212–226.

Tables

Parameter	Minimum	Maximum
H	5 km	100 km
μ'	0.01	0.6
F_z	10^{10} TN/m	10^{14} TN/m
F_x	10^{10} TN/m	10^{14} TN/m
M	10^{15} N	10^{19} N
x_0	-300 km	0 km
$\Delta\rho$	600 kg/m^3	900 kg/m^3

Table 1: Parameter range searched in the numerical models described in Section 4.2. The parameter notation is explained in the text. The range of density contrast between the sediment and the mantle $\Delta\rho$ is based on the petrophysical properties of the Ghadames Basin in Underdown and Redfern [2008].

Foreland	d^2w/dx^2, 10^{-7} 1/m	F_x, TN/m	z_e, km	z_c, km	z_s, km
Algeria	1.4–4.5	1.0	31	–	3
Colombia	0.9–2.5	3.5	18	28(?)	4
South Peru	0.9–2.6	4.5	7	31	5
India	0.6–1.4	5.0	20	51	7

Table 2: Summary of the plate curvature d^2w/dx^2, in-plane force F_x, depth of extensional faulting z_e, depth of compressional faulting z_c, and sediment thickness z_s within the forelands of mountain ranges with shallow normal faulting. The range in curvature accounts for density contrasts between sediment and mantle $\Delta\rho$ of between 600 kg/m^3 and 900 kg/m^3 and were estimated using the flexural profiles in Figure 1 and Supplementary Figures 6–8. Earthquake centroid depths are all derived from body-waveform modelling and are taken from the gWFM catalogue [Wimpenny and Watson, 2020]. The depth of compressional seismicity in the Colombian foreland is uncertain, as the epicentral uncertainty on the location of the compressional earthquake means it could be associated with a range front thrust and not be within the underthrusting Brazilian Shield. Sediment thicknesses are taken from Laske and Masters [1997].

Figures

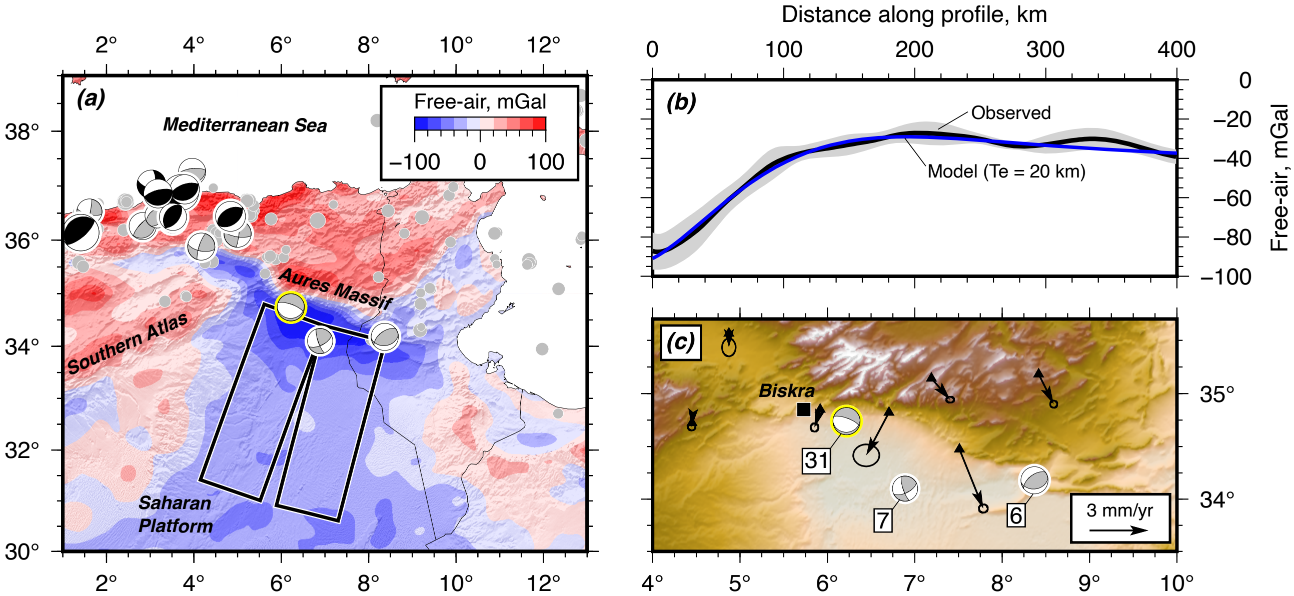

Figure 1: Overview of the 2016 Biskra earthquake. (a) Free-air gravity anomaly map derived from the EIGEN-6C gravity field [Shako et al., 2014] after applying an elliptical filter to remove signals with wavelength <50 km. Focal mechanisms in black have been derived using long-period body-waveform modelling techniques and mechanisms in grey have been derived by matching the vertical-component broadband seismograms with synthetic waveforms [Wimpenny and Watson, 2020]. Light grey circles are earthquakes with $m_b \geq 3.0$ taken from the ISC catalogue. The 2016 Biskra earthquake is highlighted in yellow. (b) Stacked profile of the free-air gravity anomalies south of the Aurés Massif taken from the black boxes in (a). A model gravity profile for an elastic plate with thickness T_e of 20 km is shown for reference. (c) Geomorphology around the Biskra earthquake. GPS velocity vectors are taken from Bougrine et al. [2019] and are shown relative to stable Nubia. Numbers next to each focal mechanisms show the earthquake centroid depth in kilometers derived from waveform modelling.

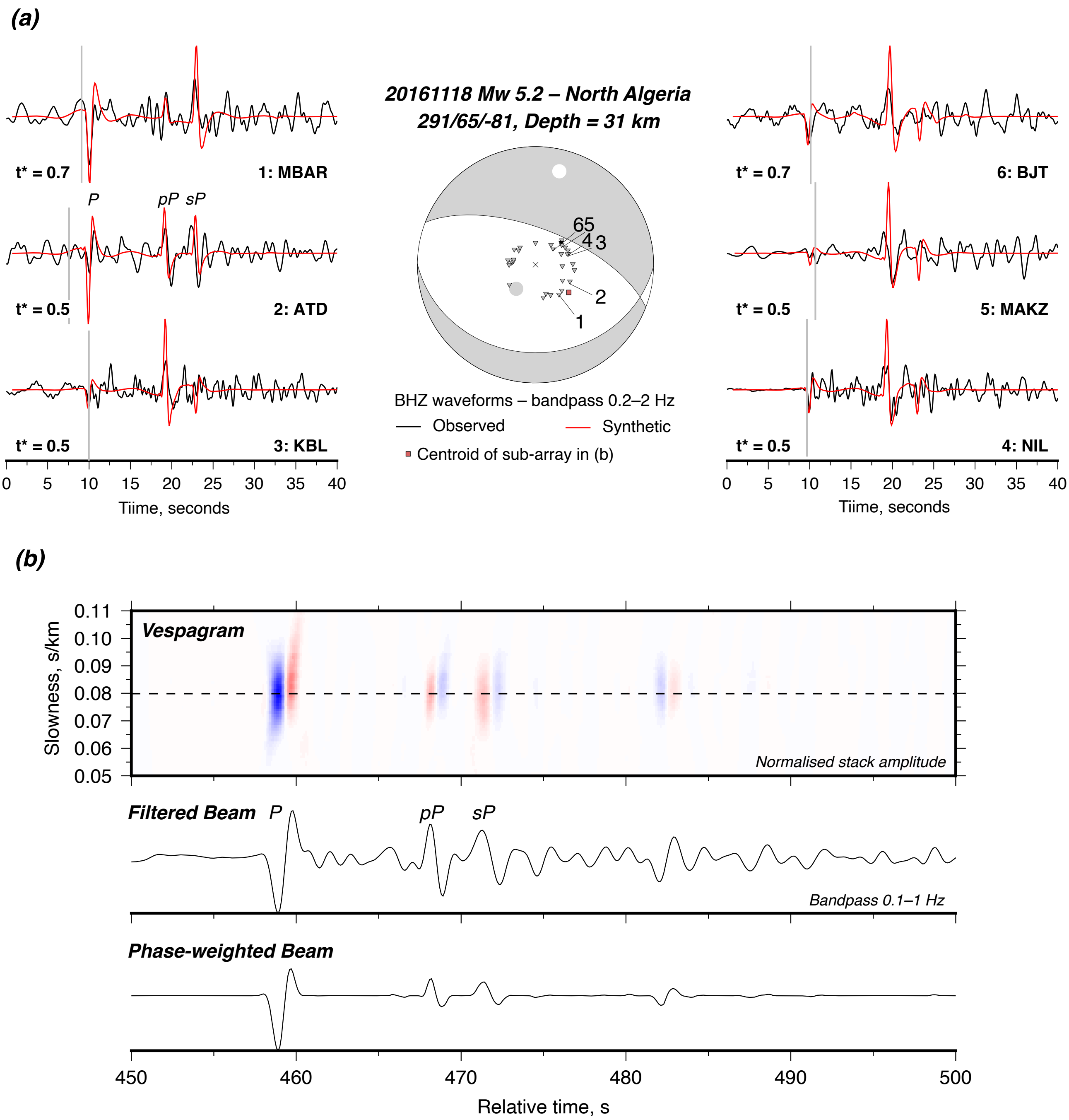

Figure 2: Teleseismic body-waveform analysis of the 18th November 2016 Biskra earthquake. (a) Forward modelling of the broadband vertical-component waveforms. The mechanism was taken from the global CMT and was updated to have a 10 degree steeper dip for the north-dipping nodal plane. The vertical gray lines on each waveform show the estimated arrival time of the direct P-phase based on the ISC hypocentral location and the IASP91 travel times. (b) Vespagram, filtered beam and phase-weighted beam for stations within a medium aperture sub-array formed of stations at 40.3 epicentral degrees demonstrating coherent arrivals 9 s and 12 s after the direct arrival, which we interpret as the pP and sP depth phases. The dashed line in the vespagram shows the slowness with peak amplitude in the stack. The centroid location of the sub-array is shown on the focal sphere in (a).

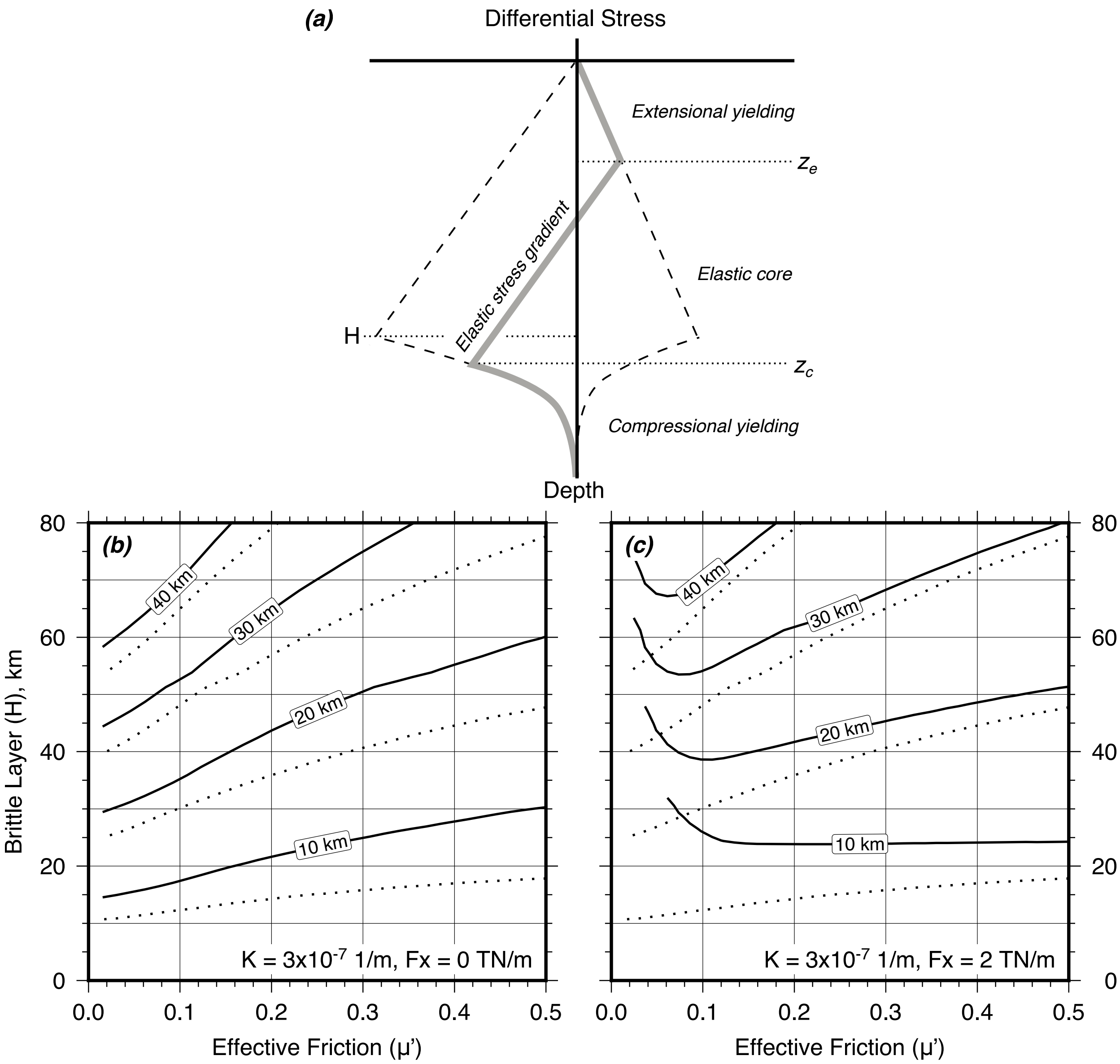

Figure 3: Semi-analytical solutions for the depth of extensional yielding within an elastic-plastic plate of curvature 3×10^{-7} 1/m. (a) Sketch of the stress distribution (thick grey line) and maximium stresses (black dashed line) supportable by the lithosphere with depth. (b) Depth of extensional yielding z_e assuming no in-plane force and a $z_r = 0$ km (solid line) or $z_r = 5$ km (dotted line). (c) Depth of extensional yielding when adding an in-plane force of $F_x = 2$ TN/m (solid line) compared to $F_x = 0$ TN/m (dotted line). All calculations in (c) assume $z_r = 5$ km.

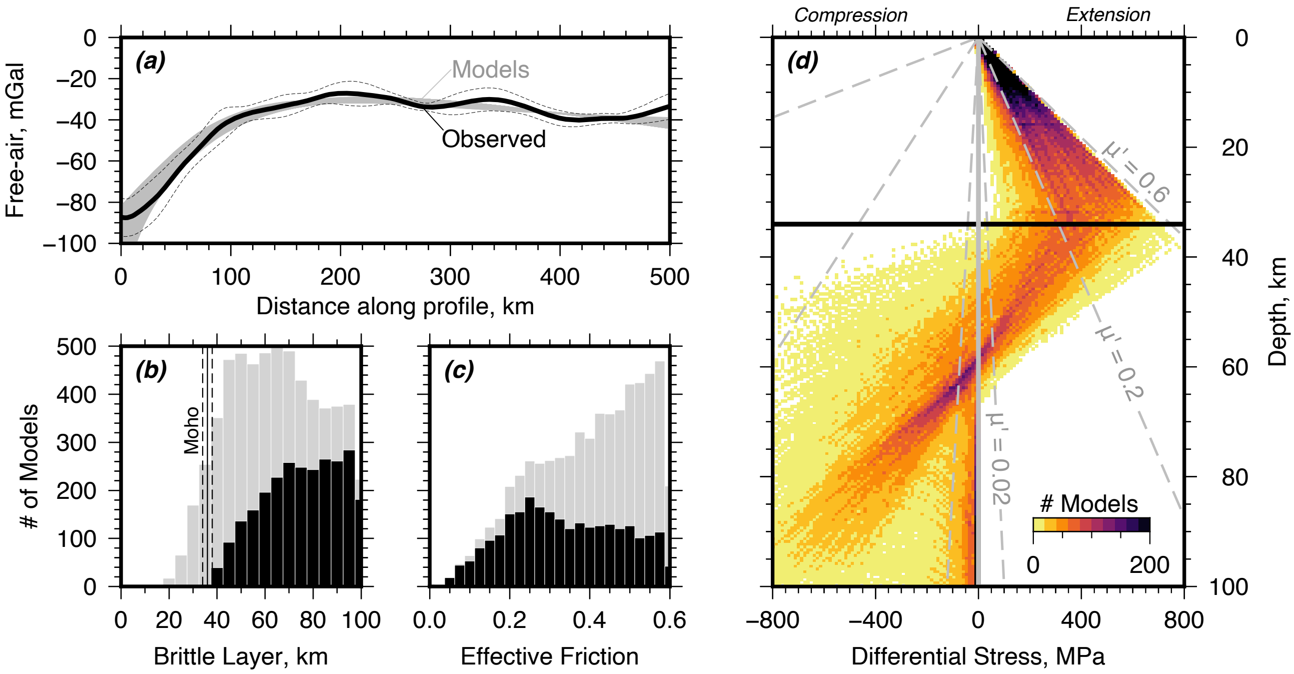

Figure 4: Results of the Monte-Carlo search for models that match the observed free-air gravity observations and the depth of extensional faulting in the Biskra earthquake. (a) Observed and modelled free-air gravity profiles for models with a $\chi^2 \leq 1.5\ \chi^2_{min}$. (b) and (c) are histograms of the brittle layer thickness (H) and effective friction (μ') for models that either fit just the gravity (grey bars), or fit both the gravity and earthquake observations (black bars). The Moho depth is taken from the seismic section of Morelli and Nicolich [1990]. (d) Differential stress within the plate taken from the location foreland-ward of the range front where the depth of extensional yielding is at a maximum. Predictions for the differential stresses needed to break faults with various μ' that dip at 45° using an average lithosphere density of 2800 kg/m^3 are shown as grey dashed lines.

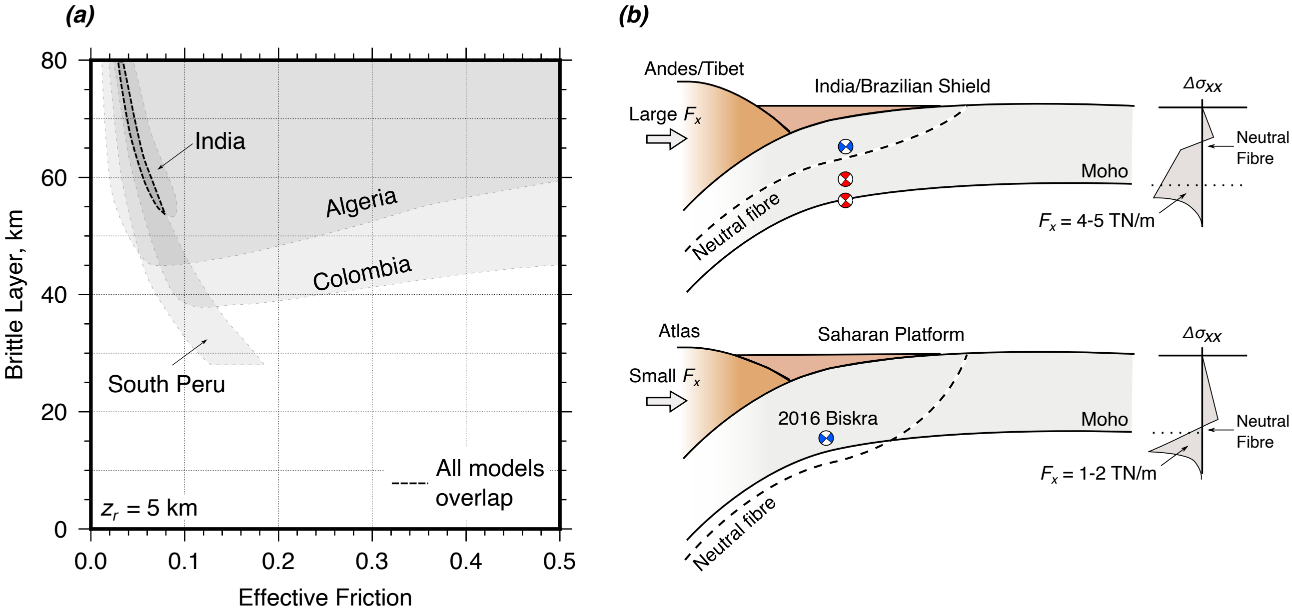

Figure 5: Summary of the differences in the depth distribution of seismicity between the Atlas, Tibetan and Andean forelands and its links with lithosphere rheology. (a) Calculations showing the range of effective friction μ' and brittle layer thickness H values that can account for the depth distribution of earthquakes, plate curvature and in-plane force in four different foreland settings. Details of the parameters used in each calculation are shown in Table 2. Each foreland is represented as a grey polygon, with darker areas showing areas where the same H-μ' combination can account for the observations from multiple foreland settings. The dashed black line shows the location in H-μ' space where a single lithosphere rheology can explain the faulting, curvature and in-plane force observations from all four settings considered here. (b) Sketch interpretation for the differences in the depth of seismicity between the forelands of the Andes, Atlas and Tibet.

Supplementary Information for: Lower-Crustal Normal Faulting and Lithosphere Rheology in the Atlas Foreland

Sam Wimpenny[1,2*], Tim Craig[1] and Alice Blackwell[1]
[1]COMET, School of Earth and Environment, University of Leeds, UK
[2]COMET, School of Earth Sciences, University of Bristol, UK
Email: *s.wimpenny@bristol.ac.uk

This Supplementary Information contains:

- **Supplementary Figure 1:** Beamforming at small-aperture arrays for the Biskra earthquake.
- **Supplementary Figure 2:** Yield stress estimates for the lithospheric mantle.
- **Supplementary Figure 3:** Sketch of the numerical model set-up.
- **Supplementary Figure 4:** Cross-plot showing the trade-offs between different model parameters in the modelling of the gravity and earthquake observations as an elastic-plastic plate.
- **Supplementary Figure 5:** Estimates of the geotherm and yield strength of the lithospheric mantle beneath the Saharan Platform.
- **Supplementary Figure 6:** Earthquakes, gravity anomalies and elastic plate model fit in India.
- **Supplementary Figure 7:** Earthquakes, gravity anomalies and elastic model fit in Colombia.
- **Supplementary Figure 8:** Earthquakes, gravity anomalies and elastic model fit in Peru.

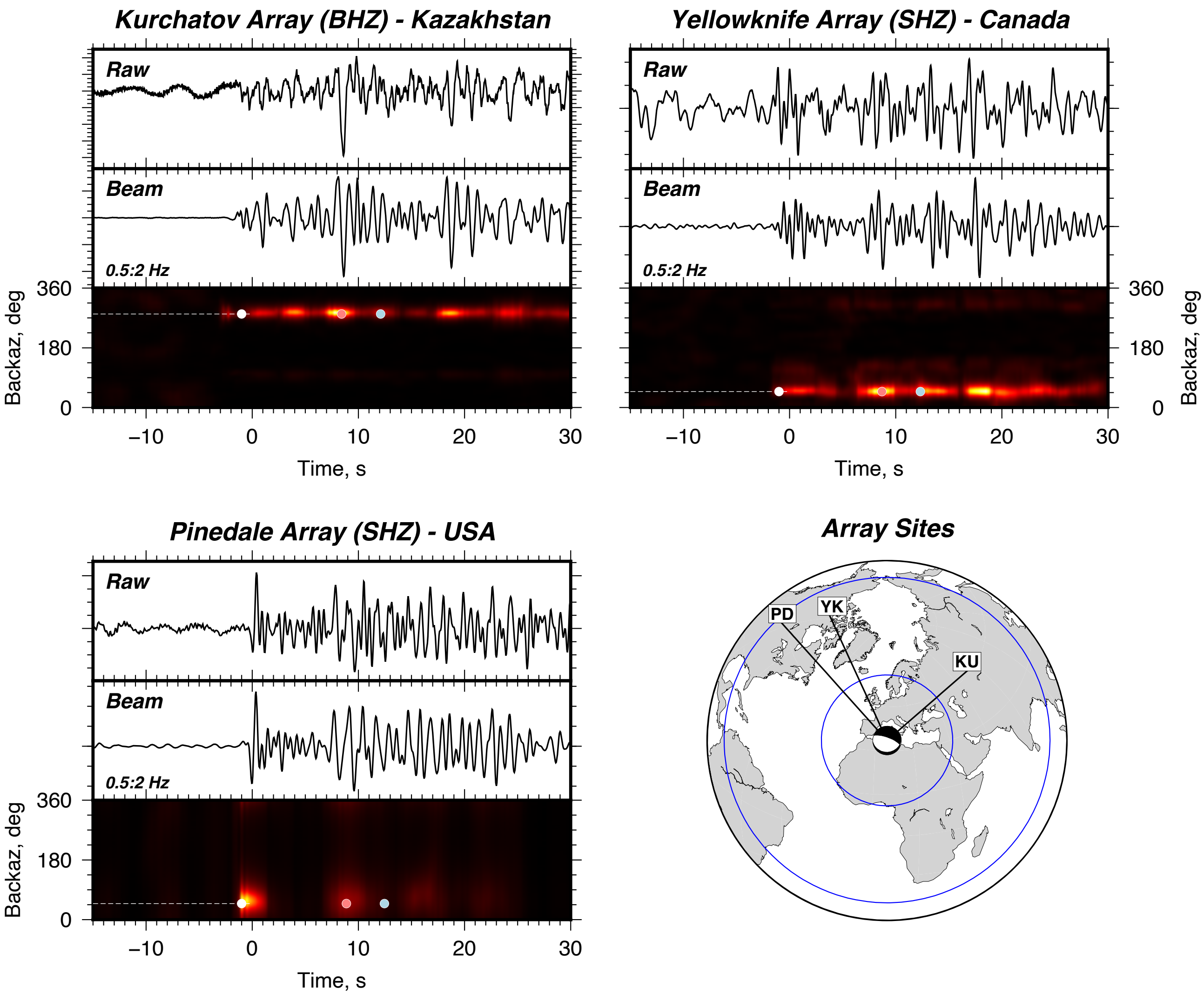

Supplementary Figure 1: Beamforming of short-period and broadband seismograms collected at small-aperture seismic arrays at teleseismic distances from the 18th November 2016 Biskra earthquake. Each panel shows a raw, unfiltered seismogram from the array, the filtered beam, and the beam amplitude as a function of back-azimuth. The white dot, red dot and blue dot represent the predicted P, pP and sP phase arrivals using a 31 km centroid depth calculated using TauP in the ObsPy package [Beyreuther et al., 2010]. The beams demonstrate that most of the energy within the P-wave coda originates from the same back-azimuth as the P-wave. Peaks in the beams can be seen particularly clearly at ∼9 seconds after the direct arrival, which is consistent with the expected arrival time of the pP phase. Energy associated with the sS arrival is less clear.

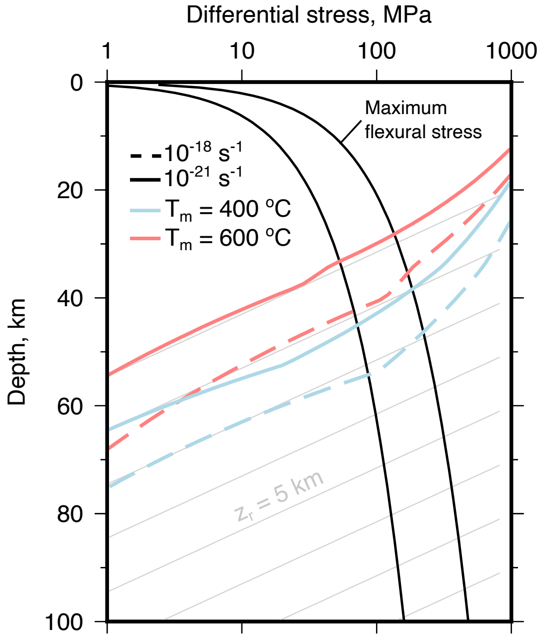

Supplementary Figure 2: Yield strength profiles for the lithospheric mantle derived from the dry olivine flow laws for dislocation creep [Hirth and Kohlstedt, 2003] and low-temperature plasticity [Mei et al., 2010]. The flow laws are shown for strain rates in the range 10^{-18} 1/s to 10^{-21} 1/s and for Moho temperatures of 400 to 600 degrees assuming a linear geotherm in crust and mantle. Predictions of the maximum flexural stress σ_f at the base of an elastic layer are shown as black lines for plate curvatures $d^2w/dx^2 = w''$ of 1–3×10^{-7} 1/m, where $\sigma_f = ETw''/2(1-v^2)$, E is the Young's modulus and v is Poisson's ratio. The grey lines show the gradient for curves of the form $\sigma \propto \exp(-z/z_r)$ where z_r is 5 km, which provide a reasonable description of the shape of the dry olivine dislocation creep flow law.

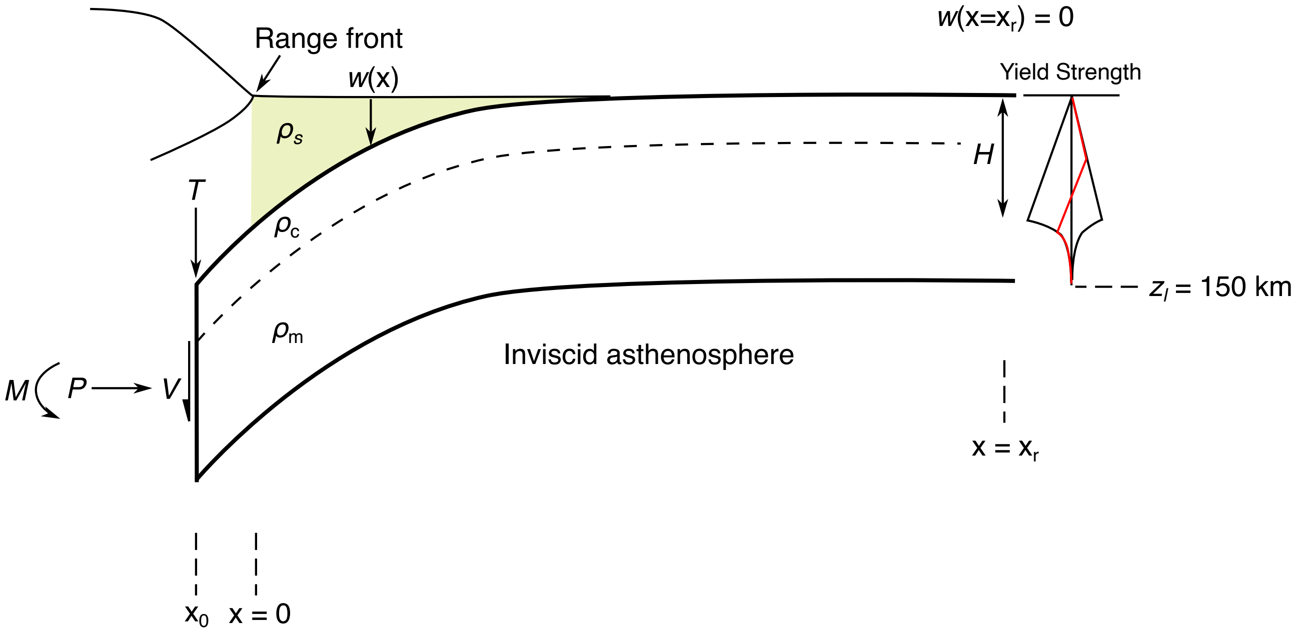

Supplementary Figure 3: Sketch of the model set-up used to calculate the stress distribution and gravity anomaly produced by lithospheric flexure using the terms defined in the main text. The left-hand boundary condition is that $V(x = x_0) = 0$. The right-hand boundary condition is that $w(x = x_r) = 0$. The co-ordinate system is relative to the range front such that $x = 0$ corresponds to the range front. The yield strength envelope follows the form $\sigma_{xx} - \sigma_{zz} = (2\mu'\bar{\rho}gz)/(\pm 1 - \mu')$ for $z < H$ and $\sigma_{xx} - \sigma_{zz} = \sigma_0 \exp(z/z_r)$ for $z \geq H$. The crustal thickness is 34 km.

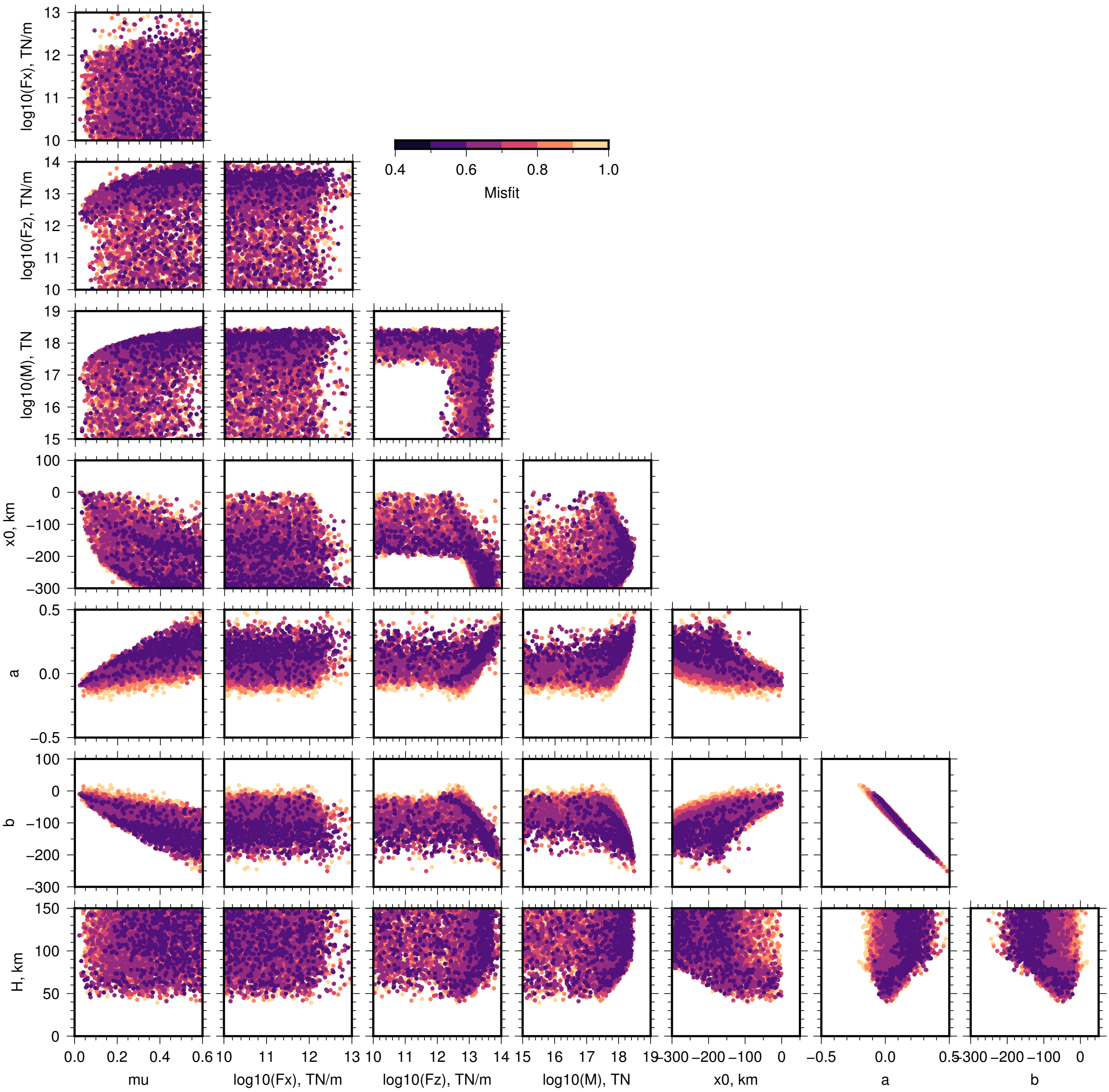

Supplementary Figure 4: Cross plots showing the trade-offs between model parameters for all of the models that matched the gravity and earthquake data shown in Figure 4 of the main text. a and b are the constants used to apply a planar ramp of the form $g(x) = g_m(x) + ax + b$ to the modelled gravity anomaly $g_m(x)$ that yields the best-fit between the modelled and observed gravity data in a least-squares sense. We do not impose any constraints on the amplitude of a or b.

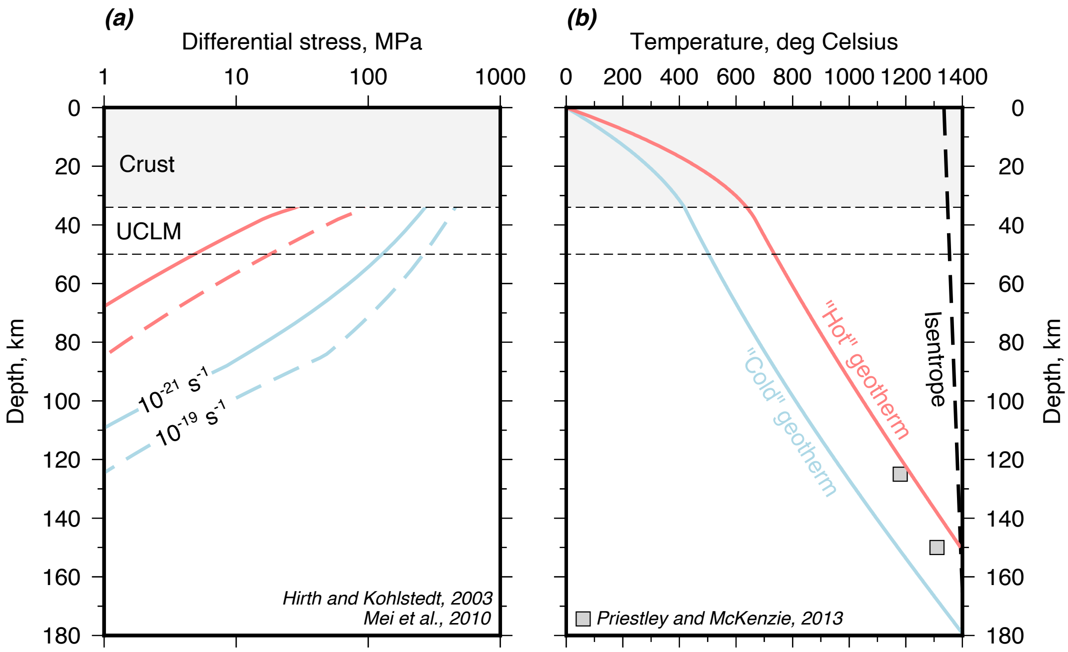

Supplementary Figure 5: Estimates of the ductile yield strength (a) for two steady-state geotherms (b) that represent upper and lower bounds on the temperature within the lithospheric mantle beneath the Saharan Platform. The differential stress is the taken as the minimum stress needed to drive deformation at the given strain rate for dry olivine using the flow laws for dislocation creep of Hirth and Kohlstedt [2003] and for low-temperature plasticity from Mei et al. [2010]. The geotherms were calculated using the method described in McKenzie et al. [2005]. For the cold geotherm, the crust is assumed to be 34 km thick and have a crustal radiogenic heat production of 0.8 μWm^{-2} and a 180 km-thick lithosphere, whilst the hot geotherm has a 38 km-thick crust, crustal radiogenic heat production of 1.5 μWm^{-2} and a 150 km-thick lithosphere. Mantle temperature estimates derived from the shear-wave velocity model of Priestley and McKenzie [2013] are shown as grey squares in (b). These simple calculations demonstrate that the the lithospheric mantle may be able to support differential stresses of a few 10's of MPa up to 50 km below the Moho at the axial strain rates associated with the underthrusting of the Saharan Platform beneath the Atlas.

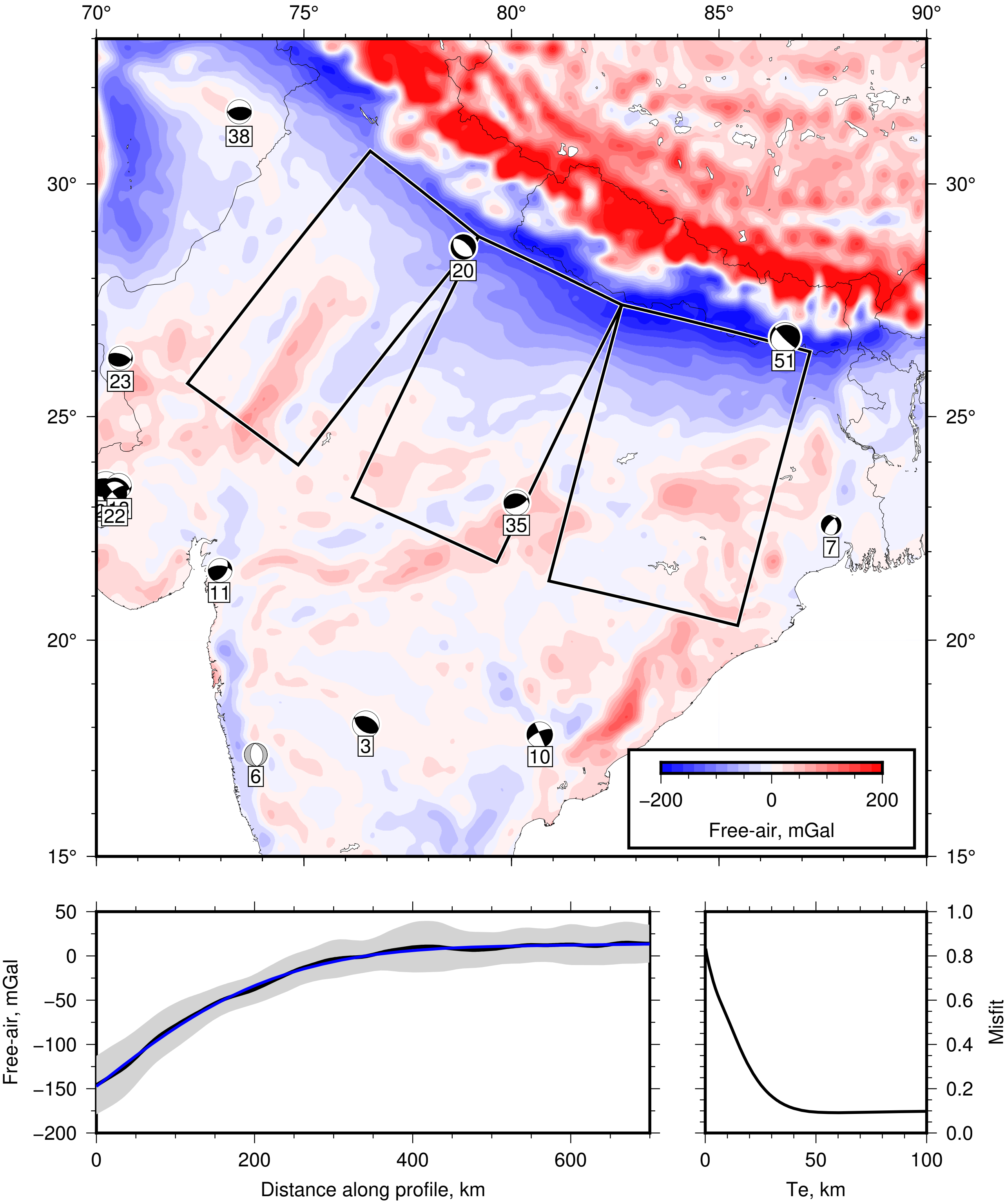

Supplementary Figure 6: Foreland seismicity and free-air gravity anomalies in the Ganges Basin of India. Earthquake mechanisms and centroid depths are taken from the Global Waveform Modelled Earthquake Catalogue [Wimpenny and Watson, 2020]. The Stacked profile of the free-air gravity perpendicular to the mountain range (black line) and the best-fit elastic plate model (blue line) are shown on the bottom left. The misfit between the elastic plate model and the free-air gravity anomaly as a function of effective elastic thickness T_e is shown on the bottom right. The misfit is calculated using the forward-modelling approach of McKenzie and Fairhead [1997]. The maximum plate curvature was calculated from the elastic plate model as 0.6–1.4 $\times 10^{-7}$ 1/m assuming density contrasts between sediment and mantle between 600 kg/m^3 and 900 kg/m^3.

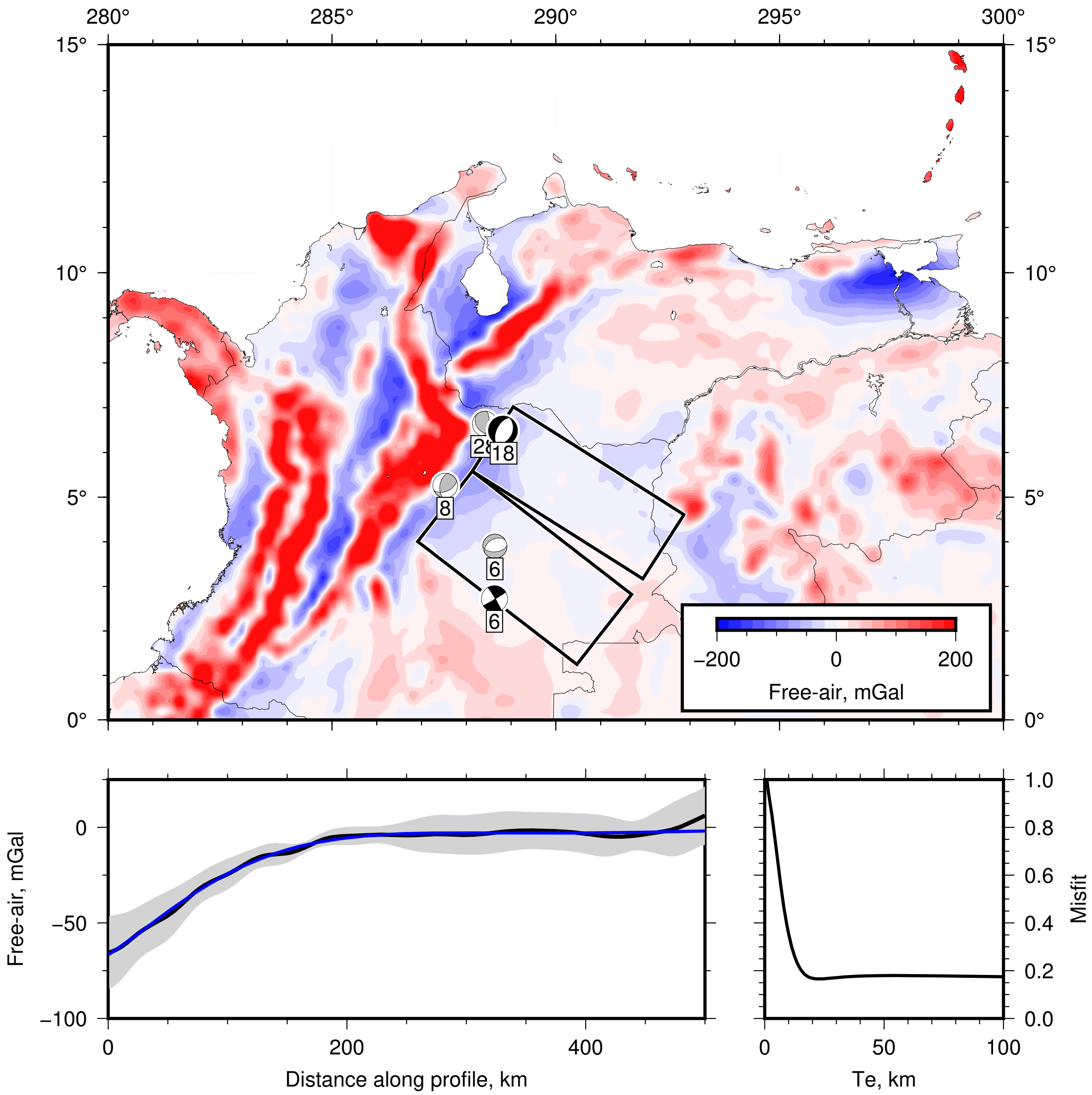

Supplementary Figure 7: Foreland seismicity and free-air gravity anomalies in the Colombian Llanos Basin (updated from Wimpenny et al. [2018]). The figure follows the same format as Supplementary Figure 6. The maximum plate curvature is 0.9–2.5 $\times 10^{-7}$ 1/m assuming density contrasts between sediment and mantle between 600 kg/m^3 and 900 kg/m^3. The depth of compressional faulting within the foreland is unclear, as the 28 km deep event lies close to the range front and could well be associated with the activation of a range-bounding thrust fault.

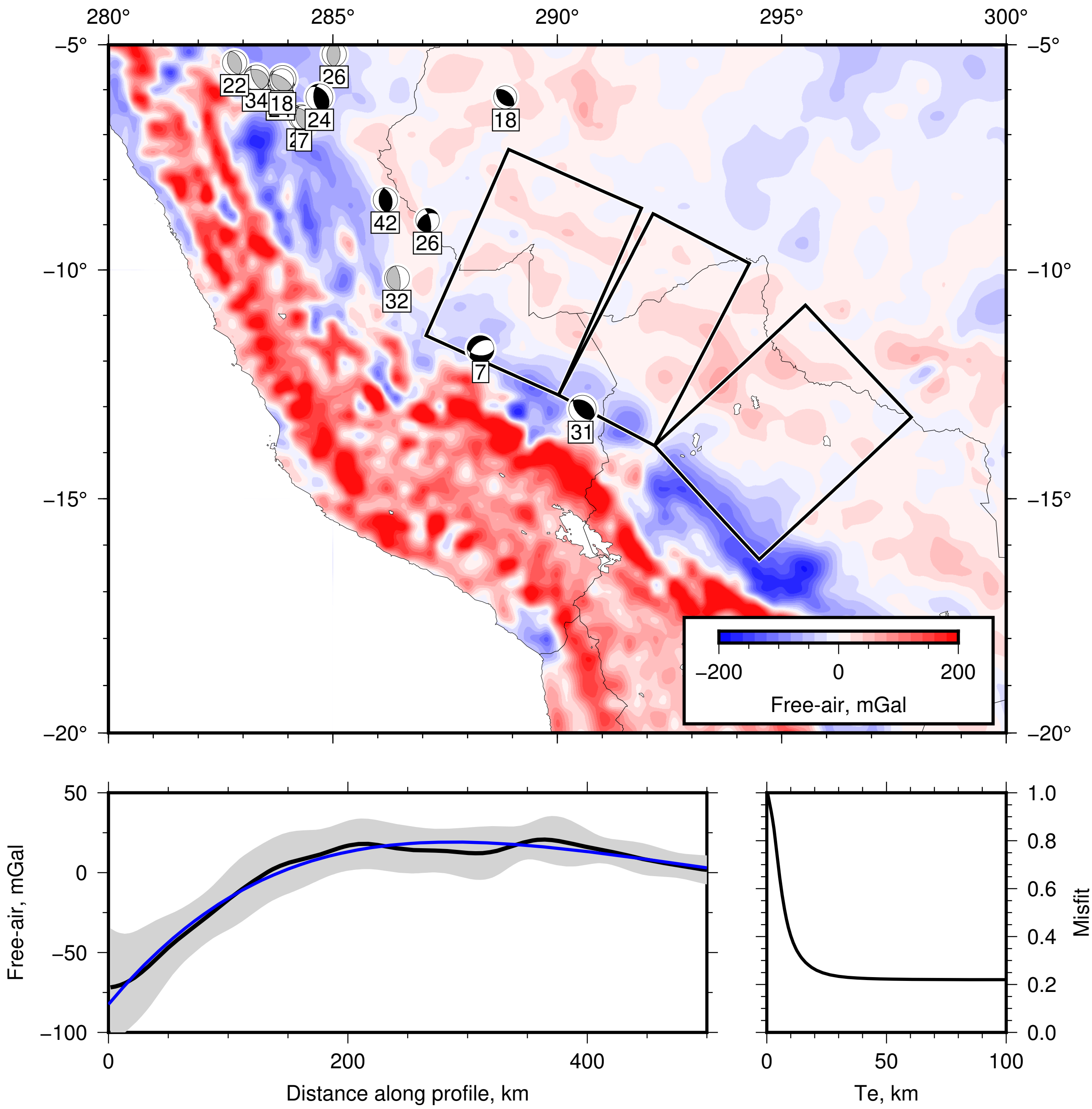

Supplementary Figure 8: Foreland seismicity and free-air gravity anomalies in southern Peru and northern Bolivia. The figure follows the same format as Supplementary Figure 6. The maximum plate curvature was 0.9–2.6 $\times 10^{-7}$ 1/m assuming density contrasts between sediment and mantle between 600 kg/m^3 and 900 kg/m^3, though we consider these estimates to be poorly constrained given the poor fit of the plate model to the gravity data.

References

Beyreuther, M., Barsch, R., Krischer, L., Megies, T., Behr, Y., and Wassermann, J. (2010). ObsPy: A python toolbox for seismology. *Seismological Research Letters*, 81(3):530–533.

Hirth, G. and Kohlstedt, D. L. (2003). Rheology of the Upper Mantle and the Mantle Wedge: a View From the Experimentalists. *Geophysical Monograph Series*, 138:83–106.

McKenzie, D. and Fairhead, D. (1997). Estimates of the effective elastic thickness of the continental lithosphere from Bouguer and free air gravity anomalies. *Journal of Geophysical Research: Solid Earth*, 102(B12):27523–27552.

McKenzie, D., Jackson, J., and Priestley, K. (2005). Thermal structure of oceanic and continental lithosphere. *Earth and Planetary Science Letters*, 233(3):337–349.

Mei, S., Suzuki, A. M., Kohlstedt, D. L., Dixon, N. A., and Durham, W. B. (2010). Experimental constraints on the strength of the lithospheric mantle. *Journal of Geophysical Research: Solid Earth*, 115(B8):B08204.

Priestley, K. and McKenzie, D. (2013). The relationship between shear wave velocity, temperature, attenuation and viscosity in the shallow part of the mantle. *Earth and Planetary Science Letters*, 381:78–91.

Wimpenny, S., Copley, A., Benavente Escobar, C. L., and Aguirre, E. (2018). Extension and Dynamics of the Andes inferred from the 2016 Parina (Huarichancara) Earthquake. *Journal of Geophysical Research: Solid Earth*, 123(9):8198–8228.

Wimpenny, S. and Watson, C. S. (2020). gWFM: A global catalog of moderate-magnitude earthquakes studied using teleseismic body waves. *Seismological Research Letters*, 92(1):212–226.